GeoScienceWorld
Lithosphere
Volume 2023, Article ID lithosphere_2023_214, 15 pages
https://doi.org/10.2113/2023/lithosphere_2023_214

Lithosphere

Research Article

Uvarovite from Reduced Native Fe-Bearing Paralava, Hatrurim Complex, Israel

Jacek Futrzyński,[1] Rafał Juroszek,[1] Katarzyna Skrzyńska,[1] Yevgeny Vapnik,[2] and Evgeny Galuskin[1]

[1]*Institute of Earth Sciences, Faculty of Natural Sciences, University of Silesia, Sosnowiec 41-205, Poland*
[2]*Department of Geological and Environmental Sciences, Ben-Gurion University of Negev, Beer-Sheva 84105, Israel*

Correspondence should be addressed to Rafał Juroszek; rafal.juroszek@us.edu.pl

Received 9 June 2023; Accepted 25 September 2023; Published 17 October 2023

Academic Editor: Marta Morana

A new genetic type of chromium garnet—uvarovite with the simplified formula $Ca_3(Cr,Al,Ti^{4+},V^{3+})_2(Si,Al)_3O_{12}$—was detected in unusual wollastonite-gehlenite-bearing paralava within the Hatrurim Complex in Israel. The pyrometamorphic rocks of that Complex usually formed in the sanidinite facies (low pressure and high temperature) and, as a rule, under oxidized conditions. This paralava contains nodules and grain aggregates of native Fe, usually distributed linearly in the rock or located close to gaseous voids. The presence of native iron droplets in association with the "meteoric" phosphide—schreibersite, suggests that the formation of paralava occurred under high-reducing conditions and high temperature, reaching 1500°C. Uvarovite forms xenomorphic grains either randomly distributed within the rock or flattened crystals on the walls of gaseous voids. Analyzed uvarovite indicates a significant enrichment in Ti^{4+} (up to 8 wt.% TiO_2) and V^{3+} (up to 4.5 wt.% V_2O_3), the highest concentrations documented for uvarovite. Unlike known uvarovite from different localities, uvarovite from this study does not contain Fe^{3+}, and Fe^{2+} is present in insignificant amounts. The obtained structural data reveal that the high contribution of hutcheonite, $Ca_3Ti^{4+}{}_2SiAl_2O_{12}$ (up to 18%), and goldmanite, $Ca_3V^{3+}{}_2Si_3O_{12}$ (up to 11%), end-members increases the lattice parameter *a* to >12.00 Å. The crystallization of uvarovite occurs in the narrow interval of oxygen fugacity, a little above the iron-wüstite buffer $fO_2 \geq \Delta IW$. Uvarovite xenomorphic grains formed due to the decomposition of wollastonite and chromite, including H_2S from the intergranular melt/fluid according to the following reaction: $Ca_3Si_3O_9 + Fe^{2+}Cr^{3+}{}_2O_4 + H_2S \rightarrow Ca_3Cr_2Si_3O_{12} + FeS + H_2O$, while the flattened crystals grew from specific melt that formed on the walls of the voids as a result of exposure of hot gas flow. The comparison of the obtained results with available chemical data from previous studies reveals a gap in the natural isomorphic series between andradite and uvarovite.

1. Introduction

Uvarovite, $Ca_3Cr_2Si_3O_{12}$, is a relatively rare member of silicate garnets, which belong to the garnet supergroup characterized by the following general chemical formula $\{X_3\}[Y_2](Z_3)\varphi_{12}$, where X, Y, and Z correspond to cationic sites, and φ is designated as an anionic site, which indicates O, OH, and F [1]. The eight-fold coordinated dodecahedral X site usually hosts divalent cations such as Mg, Ca, Mn, Fe or Na^+, and Y^{3+}; the six-fold coordinated octahedral Y site contains various cations like Mg^{2+}, Al^{3+}, $Fe^{2+,3+}$, $Mn^{2+,3+}$, V^{3+}, Cr^{3+}, Sc^{3+}, Ti^{4+}, Zr^{4+}, Sn^{4+}, Si^{4+}, Sb^{5+}, Te^{6+}, and U^{6+}; and the four-fold coordinated tetrahedral Z site is mainly occupied by Si^{4+} but also Al^{3+}, Fe^{3+}, V^{5+}, As^{5+}, Li^+, Zn^{2+}, or a vacancy [1, 2]. Previously, based on the traditional division, uvarovite, together with grossular, $Ca_3Al_2Si_3O_{12}$, and andradite, $Ca_3Fe_2Si_3O_{12}$, was subsumed into the *ugrandite series*, which contains Ca-silicate garnets characterized by different occupancies on the Y site [3]. However, the establishment of the garnet supergroup by Grew et al. [1] gives evidence to restrict the use of this term. So far, there is only one additional Cr-rich member—knorringite, $Mg_3Cr_2Si_3O_{12}$ within the garnet supergroup apart from uvarovite [4]. Nevertheless, the Cr-rich pyropes

from kimberlites [5, 6], as well as Cr-bearing grossular [7] or andradite specimens [8, 9], have also been noted. Due to the presence of a significant amount of grossular and andradite components in naturally occurring uvarovite, the pure $Ca_3Cr_2Si_3O_{12}$ end-member has not been found naturally, yet [10–12].

The range of environments in which uvarovite has been detected so far indicates a wide stability field in terms of temperature and pressure [8, 9, 13–16]. Typically, uvarovite is associated with various metamorphic rocks, especially serpentinites. It also occurs in mafic and ultramafic rocks, that is, peridotite or chromitite, which have undergone alteration due to metamorphic processes [14, 17–19]. Uvarovite was also reported in rodingites [20, 21], skarn ore deposits [22, 23], and kimberlites [24, 25]. The last documented natural occurrence, as well as in synthetic studies, indicates uvarovite stability in high-temperature and high-pressure environments [15, 16, 24]. Such a wide range of stability allows for considering uvarovite with variable composition as an important phase for geobarometry and geothermometry [13, 15, 16].

A new genetic type of uvarovite was detected in large blocks (up to 0.5 m) of wollastonite-gehlenite-bearing paralava within melilite hornfels of the Hatrurim Complex in Israel. This unusual paralava has no known equivalent, both in the Hatrurim Complex and worldwide, and it is characterized by the presence of native Fe nodules up to 1 cm in size. Here, we provide the results of uvarovite investigations within this paralava, which indicates relatively low iron contents of Fe^{2+} (0.2, 0.5 wt.% FeO) and extraordinarily high Ti and V amounts. In addition, we present data on the texture and composition of rock-forming and accessory minerals within the paralava. Moreover, the genesis of uvarovite related to the reducing conditions and crystallization from the melt involving gases is discussed, and a model of its formation is suggested.

2. Geological Settings

The Hatrurim Complex, also known as the Mottled Zone, is a geological unit located over the territory of three countries: Israel, Jordan, and Palestine (online supplementary figure S1a-b) [26–29]. It belongs to the Dead Sea-Jordan transformation tectonic system, a shear zone separating the Arabian plate from the Sinai microplate [30]. The Complex mainly consists of high-temperature, low-pressure metamorphic rocks similar by composition to Portland clinker, which formed under oxidizing conditions [26, 28, 30–32]. These rocks were classified as a product of a rare type of metamorphism—combustion metamorphism (pyrometamorphism), occurring under the sanidinite metamorphic facies [33]. The bituminous Maastrichtian to Palaeocene marls and chalks of the Ghareb and Taqiye formations, abundant in organic matter containing up to 30% organic carbon, are considered the protolith of the pyrometamorphic rocks [31, 31, 33, 34]. The most widespread pyrometamorphic rocks of the Hatrurim Complex are spurrite marbles, larnite- and gehlenite-bearing rocks, but also different paralavas characterized by a variety of mineral compositions [29, 31, 32, 35–37]. Numerous cracks, cavities, and veins usually filled by low-temperature and secondary minerals indicated the susceptibility of these rocks to late-hydrothermal alteration and weathering processes [38–41].

The formation of the Hatrurim Complex is still a matter of debate. Generally, it is accepted that sedimentary protolith, consisting mainly of carbonaceous lithologies, was metamorphosed by combustion processes. The predominant hypothesis considers formation due to the combustion of dispersed organic matter within the bitumen-rich protolith sediments [28, 38, 42]. A more recent hypothesis is related to the activity of mud volcanism, which caused metamorphic alteration due to the combustion of methane coming from the tectonically active zone of the Dead Sea Rift [27, 29].

3. Materials and Methods

3.1. Optical and Scanning Electron Microscopy. Petrographic thin sections and mount of the studied paralava with uvarovite and associated minerals were examined using a Leica DM2700P optical microscope under both transmitted and reflected light. Subsequently, studies of paralava, including semiquantitative chemical compositions of minerals and their textural relationships, were carried out using a Phenom XL scanning electron microscope equipped with an EDS (energy-dispersive X-ray spectroscopy) detector. The semiquantitative EDS analyses were performed using a high vacuum with a beam voltage of 15 kV and a working distance of 6 mm. In addition, the X-ray elemental mapping for mineral inclusions within the native Fe was made on a Quanta 250 scanning electron microscope and converted based on atomic % values. All mentioned microscopes are part of the Laboratory of Scanning Electron Microscopy at the Institute of Earth Sciences (Faculty of Natural Sciences, University of Silesia, Sosnowiec, Poland).

3.2. Electron Microprobe Analyses. Quantitative chemical analyses of minerals were performed using a CAMECA SX100 electron-microprobe operating in WDS (wavelength-dispersive X-ray spectroscopy) mode using a 15 kV acceleration voltage and 10–20 nA beam current (Faculty of Geology, University of Warsaw, Warsaw, Poland and the Polish Geological Institute, National Research Institute, Warsaw, Poland). The following X-ray lines and standards were used during the measurements: Na$K\alpha$ (albite); Ca$K\alpha$, Si$K\alpha$ and Mg$K\alpha$ (diopside); K$K\alpha$ and Al$K\alpha$ (orthoclase, sanidine); Ba$L\alpha$,$L\beta$ (baryte, celsian); Sr$L\alpha$ (celestine); Mn$K\alpha$ (rhodonite); Zn$K\alpha$ (sphalerite); Ti$K\alpha$ (rutile); Fe$K\alpha$ (Fe_2O_3 and chalcopiryte); Cr$K\beta$ (Cr_2O_3); V$K\alpha$ (V_2O_5); Co$K\alpha$ (CoO); Ni$K\alpha$ (NiO, pentlandite); Mo$L\alpha$ (molibdenite); Cu$K\alpha$ (chalcopiryte, metal Cu); S$K\alpha$ (baryte and chalcopiryte); P$K\alpha$ (apatite and YPO_4); Cl$K\alpha$ (NaCl); and F$K\alpha$ (synthetic fluorphlogopite and apatite). Due to the mineral type, size, and character of the studied crystals, the beam diameter varied from ~1 μm to 5 μm.

3.3. Single Crystal X-Ray Diffraction. Single-crystal X-ray studies of uvarovite were carried out on a four-circle Rigaku Synergy-S diffractometer equipped with a dual micro-focused source and a Hypix detector (Institute of Geological Sciences, University of Bern, Switzerland). The measurement was performed at ambient conditions, and the data were collected using Ag*Kα* radiation (λ = 0.56087 Å). The data reduction and determination of unit-cell parameters were processed using the CrystAlisPro software (Rigaku Oxford Diffraction). The crystal structure solution of uvarovite was performed in the *Ia*-3*d* space group by a direct method using the SHELXS program implemented in the WinGX software package [43, 44]. The structure was then refined using SHELXL [45]. The X (Ca1) and Z (Si1) sites were refined with calcium and silicon scattering factors, respectively, whereas for the Y site, a mixed scattering curve was used (0.729 Cr + 0.271 Al). The final structure refinement converged to R = 2.28%. Further details of data collection and crystal-structure refinement are reported in Table 1. Atom coordinates, occupancies, equivalent displacement parameters, and the main interatomic distances are listed in the CIF file, and online supplementary table S1a-c reported in Supplementary Materials.

3.4. Raman Spectroscopy. The Raman spectra of uvarovite were recorded on a WITec alpha 300R Confocal Raman microscope (Institute of Earth Sciences, Faculty of Natural Sciences, University of Silesia, Sosnowiec, Poland) using an air-cooled solid laser of 488 nm and the CCD camera operating at −61 °C. The laser radiation was coupled to a microscope through a single-mode optical fiber with a diameter of 3.5 μm. An air Zeiss (LD EC Epiplan-Neofluan DIC-100/0.75NA) objective was used. Raman scattered light was focused by an effective pinhole size of about 30 μm and a monochromator with a 600 mm^{-1} grating. The power of the laser at the sample position was 42 mW. Integration times of 5 seconds with the accumulation of fifteen scans and a resolution of 3 cm^{-1} were chosen. The monochromator was calibrated using the Raman scattering line of a silicon plate (520.7 cm^{-1}). Spectra processing, such as baseline correction and smoothing, was performed using the Spectracalc software package GRAMS. The Raman bands were fitted using a Gauss–Lorentz cross-product function with the minimum number of component bands used for the fitting process.

4. Results

4.1. Occurrence, Rock Description, and Chemical Composition. Uvarovite was found in dark paralava outcrops of the Hatrurim Complex at the east part of the Hatrurim Basin between Zohar and Halamish Wadies (Negev desert, Israel; online supplementary figure S1b-d). The rock sample has a dark color due to the presence of pyrrhotite inclusions. Areas of the rock characterized by a golden shade are enriched with microscopic perovskite inclusions (Figure 1(a)). The paralava contains aggregates and nodules of native iron up to 1 cm in size, which usually are distributed in a linear fabric in rock and are located in close proximity to the vesicles (gaseous channels), which reach up to 1 cm in diameter (Figure 1(b)). Rarely, partially replaced native Fe aggregates are observed inside gaseous channels (Figure 1(c)). Weakly altered paralava consists of long-prismatic poikilitic wollastonite crystals (several mm in length) embedded in the fine-grained crystalline groundmass of gehlenite (Figure 1(d)). Wollastonite, in rare cases, is replaced by rankinite and cuspidine. The gray, altered paralava contains an abundance of iron hydroxides and oxides substituting for sulfides and native iron. Here, a replacement of wollastonite by hydrated Ca-silicates and gehlenite by hydrogrossular is observed. Most frequently, accessory minerals in paralava are fluorapatite and chromite. Chemically, the mentioned Ca-silicates are nearly homogeneous and exhibit a composition close to the stoichiometric value (online supplementary table S2a). Only gehlenite shows minor impurities of Mg, Fe, and Na (online supplementary table S2a). Fluorapatite typically contains about 2.5 wt.% of SiO_2 (online supplementary table S2b). Chromite is characterized by dark red-brown poikilitic crystals up to 0.1 mm in length with gehlenite inclusions.

Table 1: Parameters for X-ray data collection and the crystal structure refinement of uvarovite.

Crystal data	
Empirical formula	$Ca_3Cr_{1.46}Al_{0.54}Si_3O_{12}$
Crystal system	Cubic
Space group	$Ia\bar{3}d$ (No. 230)
Unit cell dimensions	a = 12.0253(3) Å
	$\alpha = 90^{\circ}$
Unit cell volume	1738.94(12) $Å^3$
Formula weight	486.97
Density (calculated)	3.72
Z	8
Data collection	
Diffractometer	Rigaku Synergy-S
Radiation wavelength	0.56087 Å
Temperature	293(2) K
Min. and max. theta [°]	3.275–29.286
Index ranges	• -20 ≤ h ≤ 19
	• -20 ≤ k ≤ 19
	• -20 ≤ l ≤ 19
Structure refinement	
Reflections measured	14,566
No. of unique reflections	397
No. of observed unique refl. [$I>2\sigma(I)$]	305
R_{int}	0.0982
R_1	0.0228
Goof	1.103
$\Delta\rho_{min}$ [e/$Å^{-3}$]	-0.615
$\Delta\rho_{max}$ [e/$Å^{-3}$]	0.347

Its composition is similar to the following empirical crystal chemical formula $(Fe^{2+}_{0.79}Mg_{0.16}Ca_{0.02}Sr_{0.01}Mn_{0.01}Zn_{0.01})_{\Sigma 1.00}(Cr_{1.57}Al_{0.27}V_{0.08}Fe^{3+}_{0.08}Ti_{0.01})_{\Sigma 2.01}O_4$ (online supplementary table S2c).

Uvarovite, optically isotropic and green in color, forms xenomorphic grains up to 0.3 mm in size and elongated crystals up to 2 mm with inclusions of wollastonite, gehlenite, fluorapatite, and rarer chromite (Figure 2(a)–2(b)). The largest uvarovite was noted as flattened crystals up to 0.5 cm in length on the walls of gaseous channels filled with low-temperature minerals such as baryte, celestine, gypsum, calcite, hydrocalumite, tacharanite, and minerals of the ettringite-thaumasite series (Figure 2(c)–2(f)). Uvarovite is faceted by the {211}+{110} forms on the crystal side turned to the cavity space and covered by a porous red zone (Figure 2(c) and 2(f)). This zone consists of a fine mixture of iron hydroxides and sulfates with an admixture of ferric hydrogrossular.

The calculated electron microprobe (EMPA) analyses presented in Table 2 show that the compositions of uvarovite from the channel walls and xenomorphic grains in the paralava are similar (an. 1, 2, 4, Figure 3(a)–3(b)). These garnets contain 60% of uvarovite $Ca_3Cr^{3+}_2Si_3O_{12}$ end-member, 14%–18% of grossular $Ca_3Al_2Si_3O_{12}$, 8%–11% of both hutcheonite $Ca_3Ti^{4+}_2SiAl_2O_{12}$, and goldmanite $Ca_3V^{3+}_2Si_3O_{12}$ (Table 2). The highest content of the uvarovite end-member—76%, is noted in grains with chromite relicts (Table 2, an. 5). In several cases, thin rims of xenomorphic uvarovite grains are enriched in Ti (up to ~8 wt.% TiO_2), which equals 20% of the hutcheonite end-member (Table 2, an. 3). This is the highest TiO_2 content measured for natural examples of uvarovite. A similar observation has been made for the V_2O_3 constituent. The highest V_2O_3 content was equal to ~4.5 wt.% for a single analysis and >1.2 wt.% for the rest of the measured uvarovite (Table 2, Figure 3(b)). Only the crystal with the highest uvarovite end-member content incorporates less than 1 wt.% of V_2O_3 (Table 2, Figure 3(b)). The chemical formula calculation for eight cations reveals a slightly higher than $24e^-$ sum of cation charges indicating an insignificant presence of Fe^{2+} (~0.02 pfu) instead of Fe^{3+} for uvarovite from the dark paralava (Table 2).

In the analyzed paralava samples, native Fe has a rim or contains pyrrhotite and rarely cohenite Fe_3C inclusions (Figure 4(a)–4(b)). Aggregates of the Fe-P(±C) system of minerals occur even more seldomly and are characterized by the following sequence, from core to rim: iron (±cohenite)—iron with schreibersite inclusions—schreibersite-iron eutectic (Figure 4(c)). Schreibersite Fe_3P is common in meteorites but has been detected in several localities of the Hatrurim Complex in association with other so-called "extraterrestrial" mineral phases [32, 46, 47]. The compositional data show that the schreibersite contains up to 1.85 wt.% of Ni and a minor amount of Mo (up to 0.43 wt.%) and Co (up to 0.20 wt.%; online supplementary table S2d). Nickel is a main impurity in native Fe (up to 1.74 wt.%; online supplementary table S2d) and cohenite (0.6 wt.%, EDS data). Moreover, sphenoidal crystals of iron nitride ε-Fe_3N, a mineral similar to siderazote, were also identified as inclusions in native Fe (Figure 4(d), online supplementary table S2d). In addition, elemental mapping confirms high concentrations of two main elements, Fe and N, within this needle-like phase (online supplementary figure S2).

The presence of wüstite, which substitutes for native iron, was confirmed by compositional data and Raman spectroscopy (Figure 5(a); Table S2). Its xenomorphic aggregates are substituted by magnetite gradually (Figure 5(b)–5(c)) and contain pyrrhotite and tetrataenite inclusions with the following composition ~$Ni_{0.52}Fe_{0.47}As_{0.01}$ (EDS data; Figure 5(d)). However, magnetite rims around wüstite and pyrrhotite grains are usually replaced by hematite (Figure 5(b)–5(d)). Infrequently, tiny inclusions of a Fe-Ni-As-Sb alloy with different metallic ratios are also observed in magnetite (online supplementary figure S3a-c). Additionally, fine-flattened inclusions of iron hydroxides resembling an exsolution structure are noted in wüstite-magnetite pseudomorphs after native iron (online supplementary figure S3b). However, unaltered flattened inclusions are characterized by a high reflectance and a white color in BSE images (online supplementary figure S3d). The results of EDS analysis indicate iron with oxygen and carbon traces implying the formula of phase ~$Fe_3OC_{0.25}$.

Sulfides in the paralava are mainly pyrrhotite, which usually overgrows native iron, and it is replaced by later low-temperature goethite (figures 2(b); 4(b)–4(d); and 5(b)5(d)–; online supplementary table S2e). However, pyrite forms pseudomorphs after pyrrhotite and occurs in netlike pseudomorphs after an unknown sulfide (probably Ca-Fe or Ca-K-Fe sulfide, Figure 6), in which djerfisherite and isostructural zoharite were noted. These sulfides coexist and can overgrow each other, indicating changes in chemical composition (Figure 6). Zoharite is highly enriched in Ba (up to 15.06 wt.%) and Cu (up to 10.16 wt.%), and the empirical chemical formula is as follows $(Ba_{2.90}K_{2.51}Na_{0.53})_{\Sigma 5.94}(Fe_{16.89}Ni_{3.93}Cu_{3.50})_{\Sigma 24.32}S_{27.00}$ (online supplementary table S2e). In turn, djerfisherite contains almost twice as much K (up to 7.10 wt.%) and additional Cl (up to 1.23 wt.%), resulting in the composition $(K_{4.52}Ba_{0.81}Na_{0.41}Ca_{0.04})_{\Sigma 5.78}(Fe_{18.84}Ni_{4.22}Cu_{1.01})_{\Sigma 24.07}(S_{26.10}Cl_{0.90})_{\Sigma 27.00}$.

4.2 Crystal Structure. Generally, the crystal structure of cubic garnet consists of alternating YO_6 octahedra and ZO_4 tetrahedra connected by shared corners, forming a three-dimensional framework. The cavities enclosed between this framework are filled by X cations forming XO_8 dodecahedra. The garnet structure can be presented as a layered or zig-zag arrangement created by alternating edge-sharing polyhedra and octahedra, between which tetrahedra occur (Figure 7(a)) [1]. Each O atom in the structure is tetrahedrally coordinated by two cations from the X, one from Y, and one from the Z sites (Figure 7(b)). Such coordination indicates a high amount of shared edges between the dodecahedra, octahedra, and tetrahedra. However, the tetrahedra and octahedra are connected only by corners (Figure 7(a)).

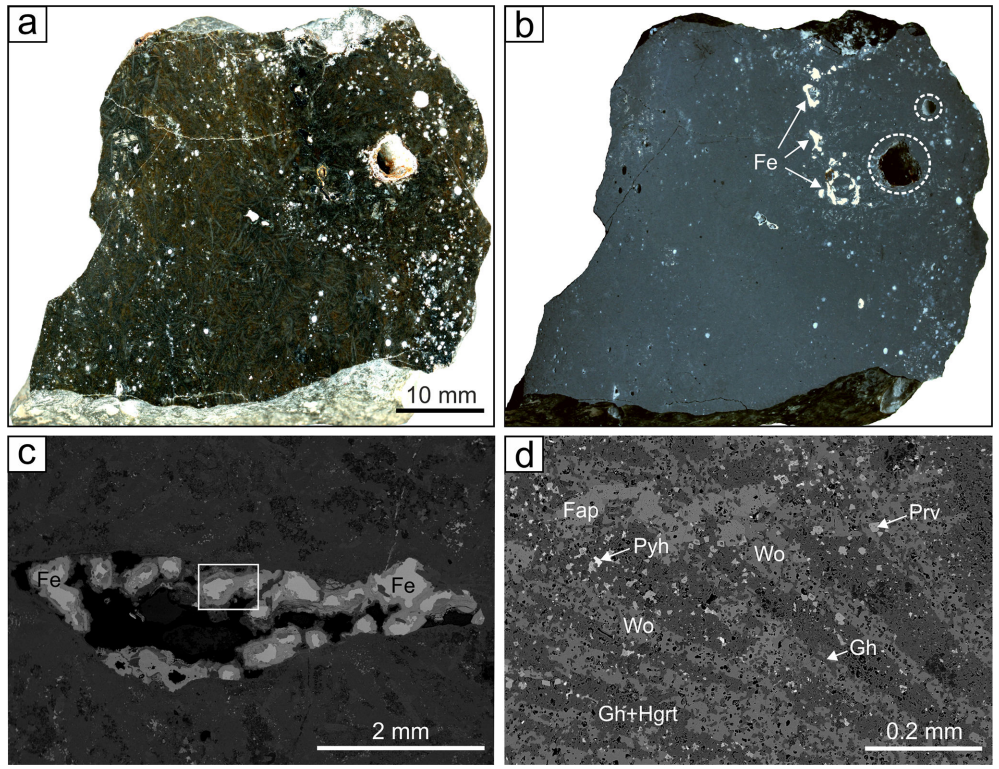

FIGURE 1: (a and b) Polished sample of wollastonite-gehlenite paralava with native Fe and gaseous channels marked by dotted lines: (a) Optical microscope image in diffused light with high contrast. The golden shade of rock with visible long-prismatic wollastonite crystals defined by perovskite inclusions. (b) An optical microscope image in reflected light. Xenomorphic grains of native iron featured by high reflectance (white). (c and d) Back-scattered electron images of native iron (white), partially replaced by wüstite and magnetite (gray) in the gaseous channel (c). The inset section is magnified in Figure 5a. The paralava sample composed of long-prismatic wollastonite crystals embedded in a fine-grained gehlenite groundmass partially replaced by hydrogrossular (d). Abbreviations: Fe, native iron; Fap, fluorapatite; Gh, gehlenite; Hgrs, hydrogrossular; Prv, perovskite; Pyh, pyrrhotite; Wo, wollastonite.

For the structural refinement, the crystal from a series of grains with the mean composition $Ca_{3.00}(Cr_{1.24}Al_{0.36}Ti^{4+}_{0.22}\ V^{3+}_{0.14}Fe^{2+}_{0.02}Mg_{0.02})_{\Sigma 2.00}(Si_{2.85}Al_{0.15})_{\Sigma 3.00}O_{12}$ was used (Table 2, analysis 1). In the obtained uvarovite structure, the X site is fully occupied by Ca cations and surrounded by eight O atoms. The interatomic distances for the dodecahedron (Ca-O) range from 2.3548(7) Å to 2.5045(7) Å. The Si cation centers the tetrahedrally coordinated Z site, and the average Si-O distances are equal to 1.6574(7) Å. This distance is scarcely more than the standard Si-O = 1.64 Å bond [48] and is connected with the substitution of Si by Al. The population refinement of the octahedral position converges at 0.729(6) Cr and 0.271(6) Al and is responded to the electron density 21.02e$^-$ and gives the mean distance of Y-O = 1.9873(7) Å (online supplementary table S1c). These values are similar to those calculated using the empirical formula with an electron density = 21.73e$^-$ and a theoretical distance of Y-O = 1.984 Å [48], as well as the Y-O = 1.985 Å bond distance value reported for the natural uvarovite sample in the previous publication [11]. The obtained structural data of uvarovite from paralava indicate that the lattice parameter a = 12.0253(3) Å is the biggest of all recorded so far, which usually varies from 11.92 to 11.97 Å [49], or is close to ~12.00 Å [11]. In the presented case, the increase of this parameter is connected with an unusually high contribution of hutcheonite $Ca_3Ti^{4+}_2SiAl_2O_{12}$ (up to 18%) and goldmanite $Ca_3V^{3+}_2Si_3O_{12}$ (up to 11%) end-members in the uvarovite composition (Table 2).

4.1.1 Raman Spectroscopy. According to the detailed factor group analysis of the garnet group minerals, twenty-five Raman active modes: 3 $_{A1g}$, 8E_g, and 14 $_{F2g}$, are expected. However, it is usually difficult to observe all of them in one spectrum [50–57]. Raman modes for silicate garnet can be divided into two high- and low-energy groups. Internal (high energy) modes contain Si-O stretching (ν_1 and ν_3) and bending (ν_2 and ν_4) vibrations of the $(SiO_4)^{4-}$ tetrahedra. On the other hand, external (low energy) modes include rotational and translational vibrations of the $(SiO_4)^{4-}$ structural unit and translational vibrations of Ca or X^{2+} dodecahedral cations [52, 53, 56, 57]. The vibrations related to the Y site cations are inactive in Raman spectroscopy [50, 52, 57].

Raman spectroscopy performed for two uvarovite crystals detected within the wollastonite paralava revealed the presence of twenty-two active bands for crystal I (Figure 8(a), Table 3) and twenty-three for crystal II (Figure 8(b), Table 3), respectively. For a more accurate interpretation, the Raman spectra presented in Figure 8 were divided into

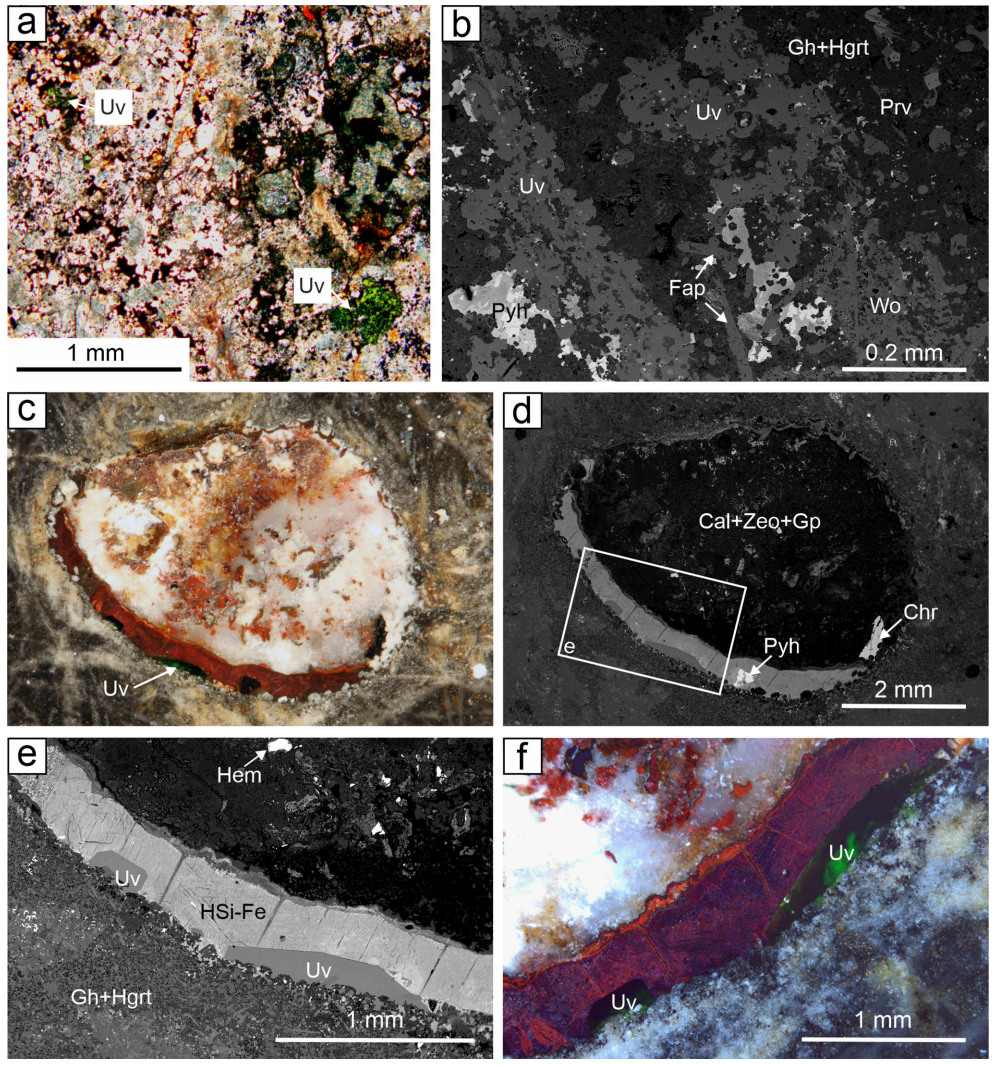

FIGURE 2: (a) Xenomorphic grains of bright-green uvarovite in transmitted light. (b) Back-scattered electron (BSE) image of elongated aggregates of uvarovite formed due to wollastonite substitution. (c and d) A gaseous channel filled with secondary minerals and flattened uvarovite crystals covered by iron hydroxides (red) on a channel wall; (c) polarized reflected light, in high contrast; (d) BSE image. The inset section is magnified in Figure 2e. (e and f) Uvarovite crystals faceted from the channel side and characterized by xenomorphic surface from the wall side covered by sulfide layer replaced by hydrated Fe-silicates, iron hydroxides, and sulfates; (e) BSE image; (f) polarized reflected light image. Abbreviations: Cal, calcite; Chr, chromite; Fap, fluorapatite; Gh, gehlenite; Gp, gypsum; Hem, hematite; Hgrs, hydrogrossular; HSi-Fe, Fe-hydro silicate + Fe-hydroxide + Fe-sulfate; Prv, perovskite; Pyh, pyrrhotite; Uv, uvarovite; Wo, wollastonite; Zeo, zeolite.

three wavenumber regions in the following ranges: 100–460 cm^{-1} (low frequency), 460–670 cm^{-1} (medium frequency), and 750–1000 cm^{-1} (high frequency). A few low-intensity Raman bands are noted for both spectra in a low wavenumber region around 170–300 cm^{-1}. The bands at 172 cm^{-1} for the I and 176 cm^{-1} for the II crystal are related to the translational vibration of the $(SiO_4)^{4-}$ group. In turn, bands in the range 220–300 cm^{-1} are assigned to the translation modes of the Ca cations at the dodecahedron sites (Figure 8). The spectral range between 300 and 460 cm^{-1} is associated with the rotational vibrations of $(SiO_4)^{4-}$. Both spectra are dominated by a very intense Raman band characterized by vibration modes of A_{1g} symmetry at 361 cm^{-1} (I) and 364 cm^{-1} (II). However, some additional bands of $(SiO_4)^{4-}$ rotational vibrations are hidden under the dominant one, and others appear near 450 cm^{-1} (Figure 8, Table 3).

For both uvarovite crystals, six Raman bands are located in the spectral range between 460 and 670 cm^{-1} (Figure 8), which are assigned to the symmetric (ν_2) and asymmetric (ν_4) vibrations of O-Si-O bending modes. An intense peak at 520 cm^{-1} (I) and 522 cm^{-1} (II) with A_{1g} symmetry surrounded by several Raman bands with E_g and F_{2g} symmetries also characterizes this frequency region (Figure 8, Table 3). The assignment of two Raman bands placed at 716 cm^{-1} (I) and 723 cm^{-1} (II) is problematic due to the absence of similar bands in previous spectroscopic reports of uvarovite, as well as other members of the garnet group. Further investigation is needed, but the authors cannot exclude incorrect band fitting near such frequencies. Raman

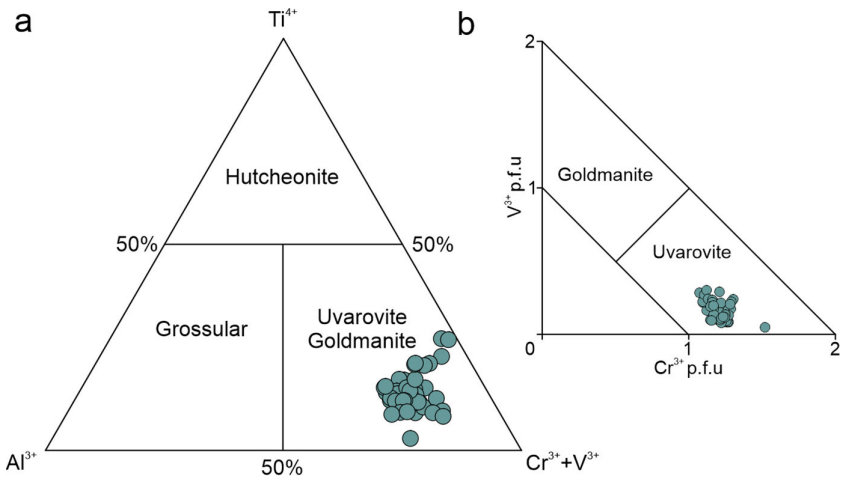

FIGURE 3: (a) Ternary diagram of the Y site cations. (b) Correlation of V^{3+} versus Cr^{3+} constructed from the results of EMPA analyses of uvarovite crystals.

spectra of the I and II uvarovite crystals show the presence of eight bands in the frequency area between 750 and 1000 cm^{-1} (Figure 8). This region is represented by Raman bands correlated with a Si-O stretching ($\nu_1 + \nu_3$) vibration of the $(SiO_4)^{4-}$ group. The asymmetric stretching vibrations (ν_3) with the E_g and F_{2g} symmetries occur at ~830 cm^{-1} and above 930 cm^{-1}. In turn, symmetric stretching vibrations (ν_1) are noted in the range of ~870–920 cm^{-1}. It was previously shown that the band near ~875 cm^{-1} is featured by A_{1g} symmetry, while the band at ~890 cm^{-1} by E_g, respectively. Moreover, the Raman bands in both spectra at 797 cm^{-1} (I) and 799 cm^{-1} (II) are related to the symmetric stretching vibrations (ν_1) of $(AlO_4)^{5-}$ with the E_g symmetry, which is connected to the partial occupancy of tetrahedral position by Al. Therefore, bands with lower intensity near ~750–760 cm^{-1} might be assigned to the asymmetric stretching vibrations of $(AlO_4)^{5-}$ groups.

The presented spectroscopic results are in agreement with previously reported data on uvarovite. The frequencies of the most intense Raman bands with A_{1g} symmetry are comparable, and the spectral ranges for the remaining vibrations were distinguished similarly [51–55]. A different number of Raman bands with regard to the literature data may be related to the detailed processing of the presented results, for example, the peak fitting process, as well as the material type and measurement conditions. The band shift to the lower or higher frequencies may be observed mainly in the high-frequency region. It can result from the occupancy of the Y site by various cations with differences in ionic radii, cation mass, and crystal field energy [53, 57]. Although the vibrations related to the Y octahedral site are not present in Raman spectroscopy, the variations within the crystal structure can lead to changes in the energy of Si-O bonds, their strength, and at the same time, the changes of band position [53, 55–57].

5. Discussion of Uvarovite Genesis

A new genetic type of uvarovite relevant to the crystallization from the melt with the assistance of hot gases was detected in the gehlenite-wollastonite-bearing paralava of the pyrometamorphic Hatrurim Complex. Two morphological types of this silicate garnet were distinguished in the analyzed samples presented in this study. The xenomorphic grains were distributed randomly in paralava, and flattened crystals formed at the channels walls. According to the chemical composition, presented uvarovite differs from their previously described counterparts due to the elevated TiO_2 and V_2O_3 contents and very low amounts of FeO (Table 2 [22, 25, 49, 58]). The enrichment in Ti observed in uvarovite from the pyrometamorphic rocks, even up to 0.5 apfu (~8 wt.% TiO_2; Table 2; Figure 3), is the highest documented for natural uvarovite. In the literature, the content of TiO_2 in uvarovite usually does not exceed 2 wt.%, and the highest content (~3 wt.%) was detected from a uvarovite grain from podiform chromitite in the Moa-Baracoa Ophiolitic Massif in Cuba [14]. A similar observation was noted in V_2O_3 content, which reaches the highest value of ~4.5 wt.% in uvarovite from the dark paralava in this study (Table 2). In comparison, only some uvarovite grains from the Cr-bearing tremolite-clinozoisite-pyrrhotite skarn occurring in northern Karelia in Finland reach as high as ~2.5 wt.% of V_2O_3 [22].

The Cr-dominant calcium garnet—uvarovite—was detected in various geological environments and different types of rocks, mainly metamorphic, such as serpentinites [8, 21], quartzites [59], skarns [22, 23], or rodingites [20, 21]. It has also been interpreted as related to the altered mafic and ultramafic rocks associated with chromite ore deposits [14, 17–19, 60]. It was also found in kimberlites, which may indicate a mantle origin [15, 16, 24]. Generally, it is assumed that a Cr-rich garnet can be formed due to a metasomatic reaction from the Cr-bearing spinel (chromite/magnesiochromite). However, the wide P-T range of uvarovite stability enables different mechanisms of crystal formations depending on the environment [13, 15, 16, 20, 21, 59]. Previous work points out the formation of uvarovite during the following different processes: (I) serpentinization at relatively low temperatures and pressure [8, 14, 17], (II) growing due to the decomposition of chromite

Table 2: Chemical composition (wt.%) of uvarovite from paralava samples derived from the Hatrurim Complex.

	1			2			3			4			5
	Mean	SD	Range	Mean	SD	Range	Mean	SD	Range	Mean	SD	Range	
	$n = 15$			$n = 9$			$n = 5$			$n = 33$			$n = 1$
Constituent				Core			Rim						Core
SiO_2	34.66	0.33	34.09–35.36	33.91	0.45	33.35–34.62	31.62	0.44	31.09–32.17	34.34	0.60	32.74–35.35	35.04
TiO_2	3.55	0.56	2.24–4.66	4.64	0.76	3.28–5.43	7.34	0.88	6.35–8.39	4.18	0.83	2.80–6.69	2.62
Al_2O_3	5.24	0.36	4.66–5.84	5.04	0.68	3.21–5.51	4.71	0.14	4.52–4.87	5.01	0.62	3.08–5.93	3.37
V_2O_3	2.08	0.55	1.25–2.81	2.44	0.75	1.27–3.78	3.12	0.09	3.06–3.29	2.66	0.98	1.19–4.54	0.72
Cr_2O_3	18.98	0.57	17.82–19.69	18.52	1.39	16.85–21.40	17.57	0.30	17.20–18.01	18.39	0.87	16.56–20.03	23.34
FeO	0.29	0.07	0.20–0.47	0.32	0.09	0.20–0.52	0.61	0.08	0.49–0.70	0.26	0.06	0.16–0.42	0.25
MgO	0.15	0.06	0.04–0.25	0.15	0.05	0.08–0.20	0.15	0.04	0.12–0.22	0.12	0.05	0.02–0.22	0.06
CaO	34.09	0.26	33.61–34.47	34.32	0.14	34.06–34.49	33.68	0.19	33.52–34.04	34.34	0.17	33.98–34.61	33.85
Total	99.04			99.34			98.80			99.29			99.17
Calculated on 8 cations													
Ca^{2+}/**X**	**3.00**			**3.00**			**3.00**			**3.00**			**3.00**
Ti^{4+}	0.22			0.29			0.46			0.26			0.16
Al^{3+}	0.36			0.28			0.10			0.31			0.23
V^{3+}	0.14			0.16			0.21			0.18			0.05
Cr^{3+}	1.24			1.20			1.16			1.20			1.52
Fe^{2+}	0.02			0.02			0.04			0.02			0.02
Mg^{2+}	0.02			0.02			0.02			0.01			0.01
Ca^{2+}	0.01			0.03			0.01			0.03			0.01
Y	**2.00**			**2.00**			**2.00**			**2.00**			**2.00**
Si^{4+}	2.85			2.79			2.64			2.82			2.90
Al^{3+}	0.15			0.21			0.36			0.18			0.10
Z	**3.00**			**3.00**			**3.00**			**3.00**			**3.00**
Charge	24.03			24.01			24.02			24.02			24.04
Uv	62			60			58			60			76
Grs	18			14			5			16			11
Htn	8			11			18			9			5
Glm	7			8			11			9			3
other	5			7			8			6			5

SD, 1σ standard deviation. *n*, number of analyses. 1,4, uvarovite crystals from the channel walls. 2, xenomorphic uvarovite grains (core). 3, xenomorphic uvarovite grains (rim) enriched in Ti. 5, xenomorphic uvarovite grain (core) with chromite relicts.

and clinopyroxenes in ultramafic host rock [60], and (III) crystallization at high pressure in a subduction zone setting by chromite and andradite reactions during the rodingitization process [21].

Available chemical analyses for natural uvarovite are shown in a ternary plot diagram (Figure 9(a)), which considers three end-members: grossular, uvarovite, and andradite, characterized by different dominant trivalent cations at the Y site. Except for Cr-bearing garnets from kimberlites, individual analyses were excluded from the population due to grossular or andradite end-member predominance. Different genetic fields of uvarovite were distinguished (Figure 9(b)), concerning the type of rocks. Considering only the relative proportion of trivalent Al, Cr, and Fe, we confirm that uvarovite from wollastonite-gehlenite-bearing paralava does not contain an andradite component as the obtained Fe amount is insignificant (~0.02 apfu; Table 2) and occurs solely as Fe^{2+}. In contrast, the uvarovite end-member reaches above 75% (Figure 9(b)). In uvarovite from rodingite-like rocks, the percentage of the uvarovite end-member is comparable to the studied uvarovite (Figure 9(b)), while andradite fluctuates between 10% and 15% [20].

Chromium and aluminum mainly occupy the Y site in the uvarovite garnets found in kimberlites. These garnets can be distinguished as intermediate members of the

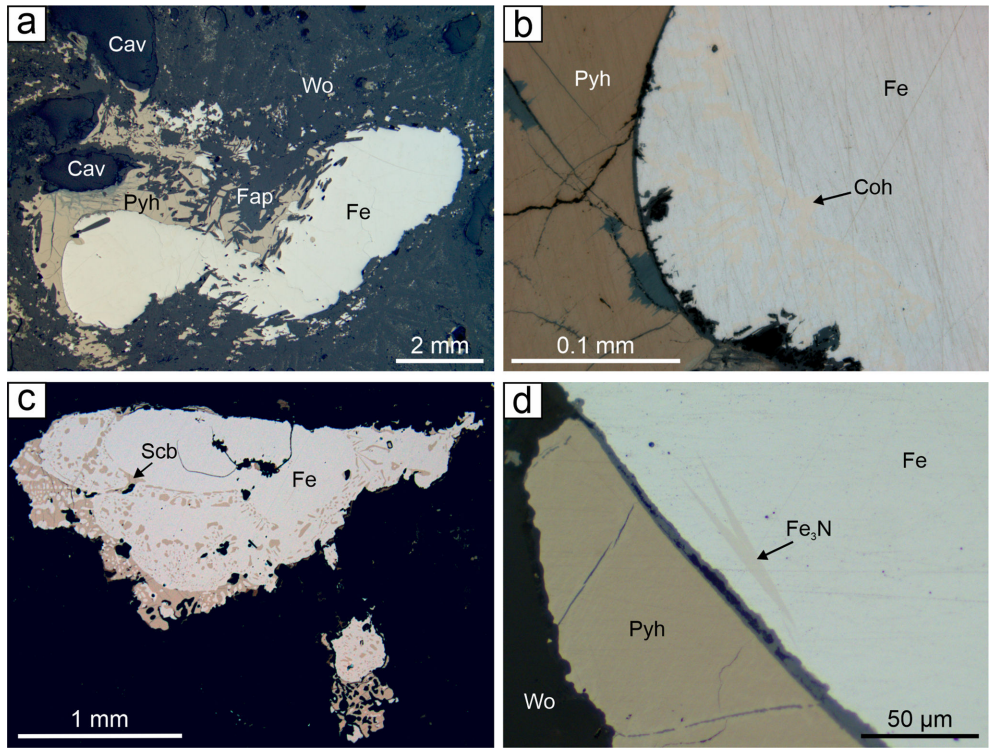

FIGURE 4: (a) A large aggregate of native iron intergrowing with pyrrhotite and fluorapatite. (b) Cohenite inclusion with a yellowish color contrasted with white native iron. (c) Native Fe with a rim of schreibersite-iron eutectic. (d) Elongate, a sphenoid-like crystal of Fe_3N phase within a native iron grain. Optical images in reflected light. Abbreviations: Cav, cavity; Coh, cohenite; Fap, fluorapatite; Fe, native iron; Fe_3N – iron nitride; Pyh – pyrrhotite; Scb – schreibersite; Wo, wollastonite.

grossular-uvarovite solid solution. Iron enrichment (up to 7.7 wt.% FeO) is also characteristic, but in this case, it occurs as Fe^{2+} and substitutes for Ca on the X site, similar to Mg^{2+}. The high amount of MgO (up to 11 wt.%) is related to the pyrope end-member $Mg_3Al_2Si_3O_{12}$ and pyrope-uvarovite coexistence in kimberlites [6, 24, 25]. Cr-dominant garnets from the Outokumpu locality (Northern Karelia, Finland) were divided based on the uvarovite composition and skarn mineral associations [22]. The main difference is noted in the Fe^{3+} content, which is the highest (up to 3 wt.% Fe_2O_3) for uvarovite crystals associated with a diopside-pyrrhotite-chalcopyrite skarn. Such Fe amounts reduced the share of the uvarovite end-member at the expense of andradite in the total composition (Figure 9(b)). The contribution of the uvarovite end-member in the remaining skarns varies between 50% and 85%, and the andradite component does not exceed 2.5% (Figure 9(b)) [22, 49].

Uvarovite garnets related to metamorphic rocks usually occur in calc-silicate rocks, such as gneiss or quartzites, and are a product of regional metasomatism [13, 23, 59, 61]. They are characterized by the most variable compositions (Figure 9(a)). The amount of the uvarovite component varies from ~50% to 80% compared with the grossular end-member in the range of 10%–40%. This uvarovite has the highest enrichment of Fe_2O_3, which reaches up to 9.5 wt.% for Cr-dominant garnet described in gneiss from Labrador [13]. The content of the calculated andradite end-member (Figure 9b), ranges from ~10% to ~32%. Uvarovite is also associated with altered igneous rocks enriched in chromitite. Usually, it appears in corroded zones next to the chromite grains or occurs within the cross-cutting veins, lenses, and lenticular bodies at contact with the surrounding rock [14, 17]. Figure 9(b) shows three fields (I–III) related to mafic igneous rocks and uvarovite garnets. The first field (I) corresponds to the type locality—Saranovskii Mine (Russia), which is hosted in dunites and harzburgites [19]. Uvarovite from this locality occurs commonly in Alpine-type veins and chemically corresponds to uvarovite from the Outokumpu skarns, characterized by slight Fe^{3+} enrichments [19, 49, 58]. The second field (II) is associated with uvarovite related to chromitite deposits, and their formation was due to metamorphic metasomatic processes [17, 62]. This uvarovite contains similar grossular and uvarovite end-member values, whereby the andradite component (13%–26%) contribution is significant (Figure 9(b)). The third field (III) is also connected with chromitite pods in which the uvarovite crystallized due to hydrothermal alteration (serpentinization) [14]. The contribution of grossular and uvarovite compounds is similar, as was noted for the second field, but the third type differs by a very low amount of Fe^{3+} (up to 0.75 wt.% Fe_2O_3).

These data confirm that the contribution of the grossular and andradite members in uvarovites is usually variable and depends on the conditions of formation and mineral paragenesis [13, 14, 21, 49, 58, 59]. Additionally, the contribution of andradite end-member is invariably below 32% in uvarovite crystals, indicating at least partially reducing conditions during uvarovite formation. It implies

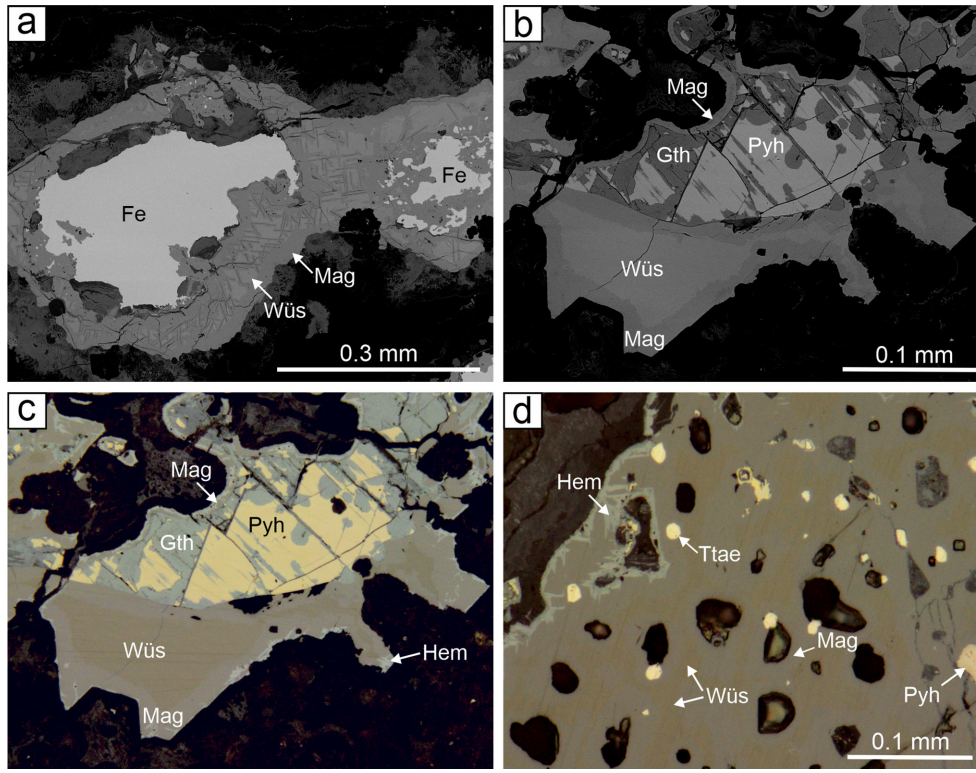

Figure 5: (a) BSE image of native iron partially replaced by wüstite and magnetite. (b and c) Intergrowth of wüstite and pyrrhotite with a characteristic rim composed of magnetite; substitution of pyrrhotite by goethite. (b) BSE image; (c) optical image in reflected light. (d) Porous wüstite grain with magnetite observed around the gas channels and small inclusions of tetrataenite and pyrrhotite distinguished by high reflectivity; optical image in reflected light. Abbreviations: Fe, native iron; Gth, goethite; Hem, hematite; Mag, magnetite; Pyh, pyrrhotite; Ttae, tetrataenite; Wüs, wüstite.

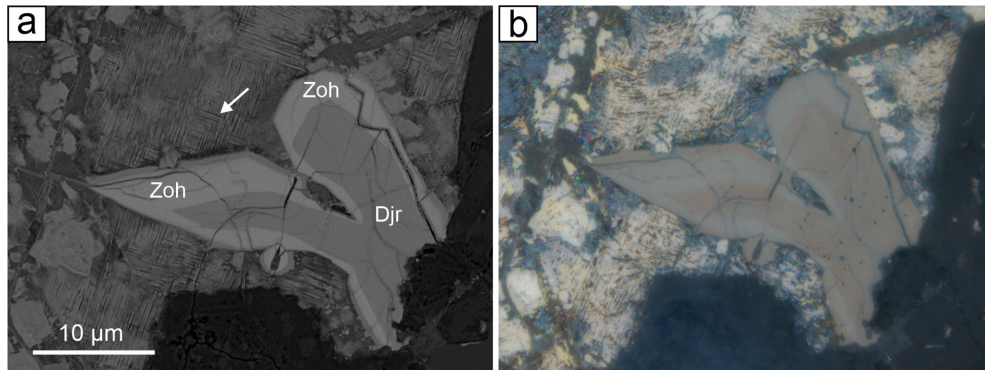

Figure 6: Zonal djerfisherite crystals with a zoharite rim in alteration products of an unknown sulfide (marked by an arrow) shown by pyrite, goethite, and iron sulfate. (a) BSE image; (b) optical image in reflected light. Abbreviations: Djr, djerfisherite; Zoh, zoharite.

the existence of a discontinuous isomorphic series between andradite and uvarovite in natural specimens.

The generation of wollastonite-gehlenite-bearing paralava in near-surface combustion foci occurred under reducing conditions at low pressures and high temperatures, which could locally reach 1500°C, confirmed by the presence of native iron droplets [32, 47, 63]. However, Raman spectroscopy data confirmed only the presence of wollastonite in the analyzed paralava, with no evidence of pseudowollastonite. That indicates the temperature during wollastonite crystallization was below 1125°C [64]. The appearance of numerous tiny drops of sulfide melt in the silicate melt results in the formation of xenomorphic pyrrhotite grains after rock-forming mineral crystallization, mainly gehlenite, and wollastonite. In rare cases, large iron melt drops probably formed after Fe-bearing mineral concretions in a sedimentary protolith. These native iron nodules are placed near or inside gaseous channels (Figure 1(b) and 1(c)), which indicates that gases can locally increase the temperature of paralava and affect iron reduction. Moreover, the zonal aggregates within the core are composed of native Fe surrounded

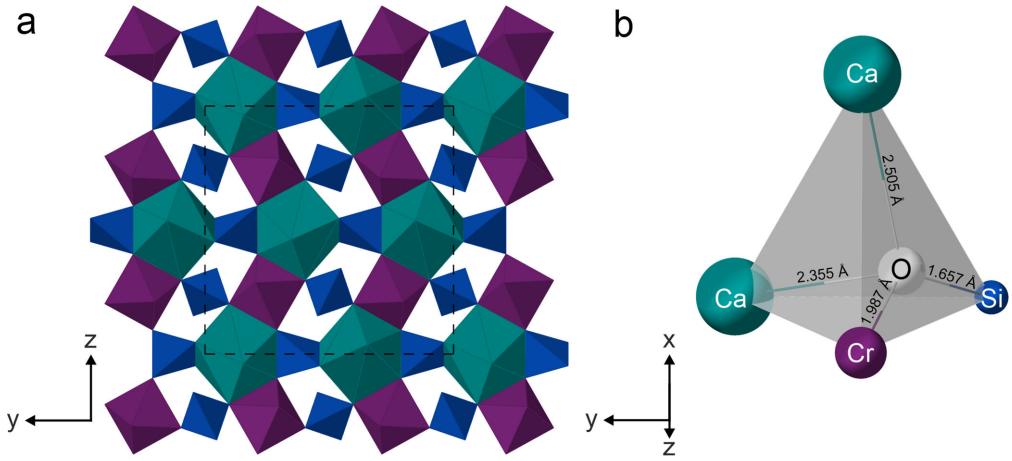

Figure 7: A slice of a uvarovite structure with a characteristic zig-zag arrangement composed of Ca-polyhedra (green) and Cr-centered octahedra (purple) linked in between by Si-tetrahedra (blue) (a). Tetrahedral coordination of oxygen atom in uvarovite structure (b).

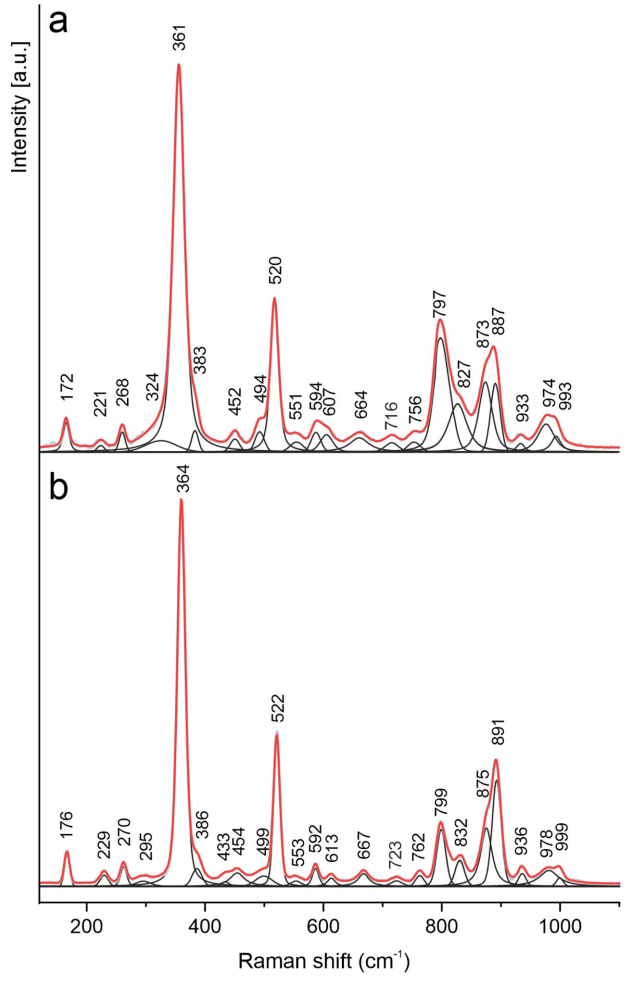

Figure 8: (a and b) Raman spectra of two uvarovite crystals from paralava samples of the Hatrurim Complex outcrops.

Table 3: Modes assignments and symmetries of the Raman active bands of the uvarovite samples.

	Uvarovite crystal I			Uvarovite crystal II		
Symmetric mode →						
Assignation ↓	A_{1g}	E_g	F_{2g}	A_{1g}	E_g	F_{2g}
Si-O stretching vibrations of $(SiO_4)^{4-}$	873	887	827	875	891	832
		933	974		936	978
			993			999
Al-O stretching vibrations of $(AlO_4)^{5-}$		797	756		799	762
O-Si-O bending vibration of $(SiO_4)^{4-}$	520	494	551	522	499	553
		594	607		592	613
			664			667
Rotational $(SiO_4)^{4-}$ modes	361	324	452	364	386	433
		383				454
Translational $(SiO_4)^{4-}$ modes		172			176	
Translational modes of Ca^{2+}			221			229
			268			270
						295

by pyrrhotite, which indicates enrichment in sulfur of the metal melt. Occasionally, sulfide nodules consisting of pyrrhotite and an altered phase (probably K-Fe or Ca-Fe sulfide) were noted, after which secondary pyrite and pseudomorphs composed of iron oxides-hydroxides with a characteristic net-like texture were formed. A change of metal nodule composition in the samples according to the following sequence: native Fe → wüstite → magnetite → hematite (Figure 5(a)–5(c)) indicates an increase in the oxygen fugacity during paralava crystallization. However, hot reducing gases (like CO, H_2, H_2S, HF, and methane) and variations of atmospheric conditions, especially around gaseous channels, could change the oxygen fugacity rapidly. Additionally, the association of native Fe with schreibersite (Figure 4(c)), which was also described in contact metamorphic facies of the gehlenite-bearing paralava of

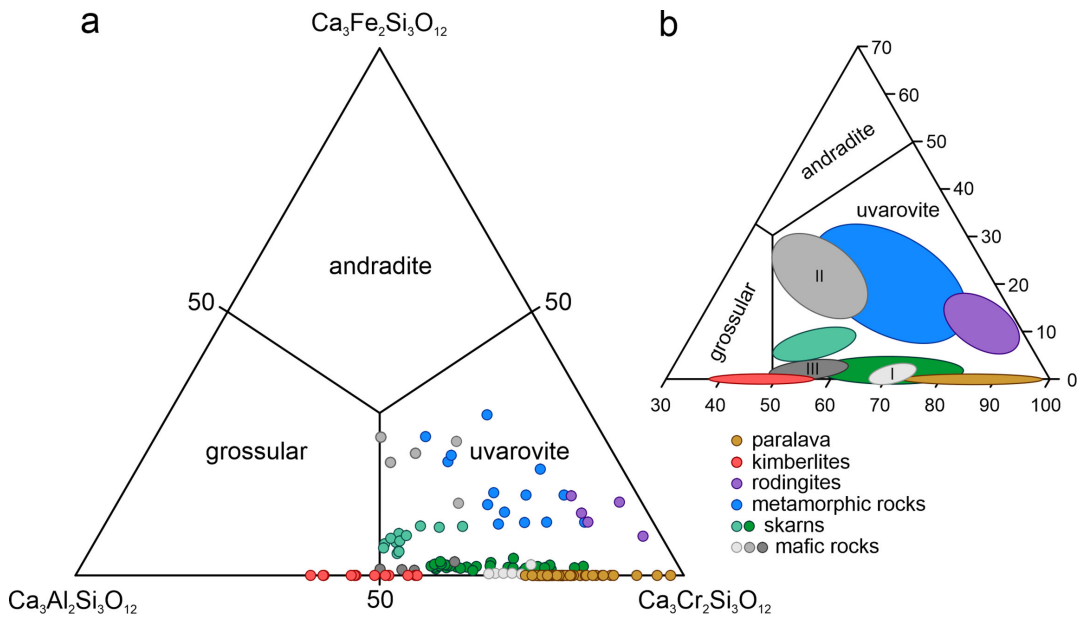

FIGURE 9: (a) Ternary plot of the Y site contents of uvarovite garnets. The Y site was calculated from the relative proportion of Cr^{3+}, Al^{3+}, and Fe^{3+} with the consideration of Al partial substitution at the Z site. (b) Fragment of the ternary diagram showing the genetic fields of uvarovite. Sources of data: [6, 13, 14, 17, 19, 20, 22–25, 49, 58, 59, 61, 62].

the Hatrurim Complex [32], indicates super-reductive conditions in the crystallization environment: $fO2 < \Delta IW = \sim -3 - -5$ (Figure 10). Schreibersite and other phosphides can be formed under low-pressure and high-temperature conditions (1200°C–1500°C) due to the carbothermal reduction process combined with the production of gaseous by-products that came from organic matter decomposition [32, 47].

Uvarovite is a relatively late mineral of paralava that crystallizes in a narrow range of the oxygen fugacity, slightly above the iron-wüstite buffer $fO_2 \geq \Delta IW$ (Figure 10) as indicated by the low Fe^{2+} content in its composition, and relatively high V^{3+} content (Table 2). The decomposition of wollastonite and chromite with the participation of H_2S can lead to the formation of xenomorphic uvarovite and pyrrhotite according to the following reaction: $Ca_3Si_3O_9 + Fe^{2+}Cr^{3+}{}_2O_4 + H_2S \rightarrow Ca_3Cr_2Si_3O_{12} + FeS + H_2O$. In addition, the texture of xenomorphic uvarovite indicates formation at the expense of wollastonite substitution, wherein the relatively low amount of such garnet in paralava is correlated with the limited content of accessory chromite (Figure 2(a)–2(b)). At the same time, flattened uvarovite crystals on the walls of channels crystallized from the silicate melt, which is confirmed by their morphology (Figure 2(c)–2(f)). This melt (thin layer) was likely formed during a short-time interval heating of the channel walls by hot gases. In places where chromite grains were present in paralava, the melt was enriched in Cr (+V), which enabled the crystallization of uvarovite. Additionally, the effect of active gaseous channels in partially crystallized paralava increased perovskite crystal size by 10–20 times in the area of their influence.

6. Conclusions

Uvarovite garnet detected in paralava samples from the pyrometamorphic Hatrurim Complex shows enrichment in Ti^{4+} up to ~8 wt.% and V^{3+}up to ~4.5 wt.%. So far, these are the highest values confirmed for natural Cr^{3+}-dominant silicate garnet. Simultaneously, the involvement of the uvarovite end-member is significant at ~75%, and it is comparable to the content of the uvarovite end-member for Cr-bearing garnet specimens occurring in rodingite-like rocks. Moreover, iron content is negligible and recorded only as Fe^{2+} in the investigated uvarovite composition. The relevant contribution of hutcheonite, $Ca_3Ti^{4+}{}_2SiAl_2O_{12}$, and goldmanite, $Ca_3V^{3+}{}_2Si_3O_{12}$, end-members indicates the increase of the unit-cell lattice parameter $a > 12$ Å, which is the largest reported for natural uvarovite. In the analyzed rock samples, uvarovite forms two morphologically different types of assemblages. The xenomorphic grains appear due to the decomposition of wollastonite and chromite with the participation of H_2S from the intergranular melt/fluid. In turn, flattened uvarovite crystals crystallized from a secondary melt formed on the walls of the channels with the interaction of hot gases. Uvarovite described in this work presents a new genetic type related to reduced conditions, indicating a narrow range of the oxygen fugacity ($fO_2 \geq \Delta IW = 1$), and crystallization from the melt involving gases. The comparison of the obtained results with available chemical data from previous studies reveals the gap in isomorphic series between andradite and uvarovite within natural samples. The presented investigation concludes that uvarovite can be an indicator of oxygen fugacity during rock formation based on the presence of Fe^{2+} and Fe^{3+} in its structure.

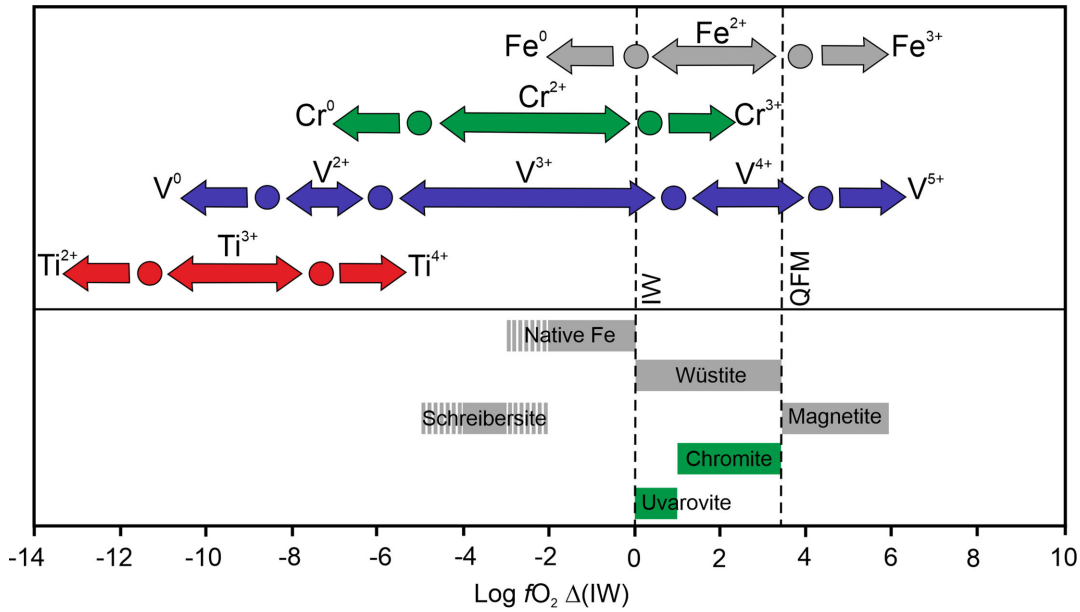

FIGURE 10: Schematic diagram of oxygen fugacity related to the wüstite-magnetite buffer and the extent of Fe- and Cr-bearing minerals detected in the paralava sample. Modified after [65].

Data Availability

All data generated or analyzed during this study are included in this published paper and its supplementary material section. Primary data are available from the corresponding author on request.

Conflicts of Interest

The authors declare that they have no conflicts of interest.

Acknowledgments

The field works and microprobe investigations were supported by the National Science Center (NCN) of Poland, grant 2021/41/B/ST10/00130. The authors thank Georgia Cametti from the University of Bern for help during the SC-XRD analyses.

Supplementary Materials

Uvarovite_Hatrurim Complex.cif file; Table S1a: Atom coordinates (x,y,z), equivalent isotropic displacement parameters (Uiso, Å2), and site occupancies of uvarovite; Table S1b: Anisotropic displacement parameters (Å2) of uvarovite; Table S1c: Selected interatomic distances (Å) of uvarovite structure; Table S2a: Chemical composition (wt.%) of rock-forming minerals detected in analyzed paralava samples; Table S2b: Chemical composition (wt.%) of fluorapatite detected in analyzed paralava samples; Table S2c: Chemical composition (wt.%) of accessory minerals related to the spinel subgroup and wüstite; Table S2d: Chemical composition (wt.%) of native Fe, Fe3N phase and schreibersite; Table S2e: Chemical composition (wt.%) of sulfides detected in analyzed paralava samples; Figure S1: (a) Schematic map of the Middle East with the Hatrurim Complex outcrops along the Israel-Jordan border; fragment outlined by frame is magnified in Figure S1b. (b) Hatrurim Basin outcrop with marked locality (red dot) of the uvarovite sampling. (c) Uvarovite locality in between Zohar and Halamish Wadies. (d) Samples of dark paralava with aggregates and nodules of native iron and uvarovite crystals; Figure S2: Elemental mapping for N, Fe, S, Ca, Si, Al and O. (a) BSE image of native Fe associated with pyrrhotite and noticeable inclusion of Fe3N phase. Figure S3: Wüstite-magnetite pseudomorphs after native iron; (a) Optical image; (b) BSE image. The framed sections are magnified in Figures S3c and d. (c) BSE image of Fe-Ni-As-Sb alloy within the magnetite. (d) BSE image of tiny needle-like inclusions of iron carbide ~Fe3OC0.25. Abbreviations: Fe – native iron; Fe3N – iron nitride; Gh – gehlenite; Hem – hematite; Mag – magnetite; Prv – perovskite; Py – pyrite; Pyh – pyrrhotite; Wo – wollastonite; Wüs – wüstite.

References

[1] E. S. Grew, A. J. Locock, S. J. Mills, I. O. Galuskina, E. V. Galuskin, and U. Halenius, "Nomenclature of the garnet Supergroup," *American Mineralogist*, vol. 98, no. 4, pp. 785–811, 2013.

[2] S. M. Antao, "Crystal structure of an Anisotropic Pyrope garnet that contains two cubic phases," *Minerals*, vol. 11, no. 12, p. 1320, 2021.

[3] A. N. Winchell, *Elements of Optical Mineralogy. An Introduction to Microscopic Petrography. Part II Descriptions of Minerals*. 3rd edition, Wiley, New York, 1933.

[4] P. H. Nixon and G. A. Hornung, "New chromium garnet end member, Knorringite, from Kimberlite," *American Mineralogist*, vol. 53, pp. 1833–1840, 1968.

[5] H. O. A. Meyer and F. R. Boyd, "Composition and origin of crystalline inclusions in natural diamonds," *Geochimica et Cosmochimica Acta*, vol. 36, no. 11, pp. 1255–1273, 1972.

[6] W. A. Deer, R. A. Howie, and J. Zussman, *Rock Forming Minerals. IA. Orthosilicates*. 2nd edition, Longman, London, 1992.

[7] P. J. Dunn, "On the composition of some Canadian green Garnets," *The Canadian Mineralogist*, vol. 16, pp. 205–206, 1978.

[8] J. M. Duke and M. Bonardi, "Chromian Andradite from Reaume Township, Ontario," *The Canadian Mineralogist*, vol. 20, pp. 49–53, 1982.

[9] M. Q. Jan, B. Windley, and R. N. Wilson, "Chromian Andradite and Olivine-chromite relations in a Chromitite layer from the Jijal complex, Northwestern Pakistan," *Canadian Mineralogist*, vol. 22, pp. 341–345, 1984.

[10] G. Menzer, "Die Kristallstruktur der Granate," *Zeitschrift Für Kristallographie - Crystalline Materials*, vol. 69, nos. 1–6, pp. 300–396, 1929.

[11] G. A. Novak and G. V. Gibbs, "The crystal chemistry of the silicate Garnets," *American Mineralogist*, vol. 56, pp. 791–825, 1971.

[12] H. Sawada, "Elect$_R$on density study of Garnets: ca$_3$(Cr,Al)$_2$Si3O12," *Journal of Solid State Chemistry*, vol. 132, no. 2, pp. 432–433, 1997.

[13] R. Kalamarides and J. Berg, "Coexisting Cr-rich and Cr-poor garnet from a Calc-silicate gneiss, Labrador," *Canadian Mineralogist*, vol. 26, pp. 335–342, 1988.

[14] J. Proenza, J. Sole, and J. C. Melgarejo, "Uvarovite in Podiform Chromitite; the Moa-Baracoa Ophiolitic Massif, Cuba," *The Canadian Mineralogist*, vol. 37, pp. 679–690, 1999.

[15] S. Klemme, J. C. V. Miltenburg, P. Javorsky, and F. Wastin, "Thermodynamic properties of Uvarovite garnet (Ca3Cr$_2$SI$_3$O1$_2$)," *American Mineralogist*, vol. 90, no. 4, pp. 663–666, 2005.

[16] S. Gréaux and A. Yamada, "Density variations of Cr-rich Garnets in the upper Mantle inferred from the elasticity of Uvarovite garnet," *Comptes Rendus Geoscience*, vol. 351, nos. 2–3, pp. 95–103, 2019.

[17] J. J. Frankel, "Uvarovite garnet and South African jade (Hydrogrossular) from the Bushveld complex, Transvaal," *American Mineralogist*, vol. 44, pp. 565–591, 1959.

[18] K. L. Chakraborty, "Mineralogical note on the chrome-Chlorite (Kämmererite) and chrome-garnet (Uvarovite) from the chromite deposits of Kalrangi, Orissa, India," *Mineralogical Magazine and Journal of the Mineralogical Society*, vol. 36, no. 283, pp. 962–965, 1968.

[19] E. M. Spiridonov, M. S. Alferova, and T. G. Fattykhov, "Gem minerals from the Saranovskoye chromite deposit, Western Urals," *The Journal of Gemmology*, vol. 30, no. 1, pp. 91–102, 2006.

[20] A. Mogessie and D. Rammlmair, "Occurrence of zoned Uvarovite-Grossular garnet in a Rodingite from the Vumba Schist belt, Botswana, Africa: implications for the origin of Rodingites," *Mineralogical Magazine*, vol. 58, no. 392, pp. 375–386, 1994.

[21] C. Zhang, T. Shen, L. Zhang, et al., "The formation and evolution of Uvarovite in UHP Serpentinite and Rodingite and its constraints on chromium mobility in the Oceanic Subduction zone," *Acta Geologica Sinica - English Edition*, vol. 95, no. 5, pp. 1456–1471, 2021. https://onlinelibrary.wiley.com/toc/17556724/95/5.

[22] O. von Knorring, E. Condliffe, and Y. L. Tong, "Some mineralogical and Geochemical aspects of chromium-bearing Skarn minerals from northern Karelia, Finland," *Bulletin of the Geological Society of Finland*, vol. 58, no. 1, pp. 277–292, 1986.

[23] Y. Pan and M. E. Fleet, "Cr-rich Calc-silicates from the Hemlo area, Ontario," *Canadian Mineralogist*, vol. 27, pp. 565–577, 1989.

[24] N. V. Sobolev, Yu. G. Lavrent'ev, N. P. Pokhilenko, and L. V. Usova, "Chrome-rich Garnets from the Kimberlites of Yakutia and their Parageneses," *Contributions to Mineralogy and Petrology*, vol. 40, no. 1, pp. 39–52, 1973.

[25] S. M. Sablukov, L. I. Sablukova, and Y. B. Stegnitskiy, "New mineralogical type of Mantle substrate (Nakyn Kimberlite field, Yakutia, " in *Proceedings of the Alkaline Rocks, Kimberlites and Carbonatites: Geochemistry and Genesis*, N. Vladykin, Ed., pp. 181–209, Springer International Publishing, 2021.

[26] S. Gross, "The Mineralogy of the Hatrurim formation, Israel," *Geological Survey of Israel*, vol. 70, 1977.

[27] E. Sokol, I. Novikov, S. Zateeva, Ye. Vapnik, R. Shagam, and O. Kozmenko, "Combustion Metamorphism in the Nabi Musa Dome: new implications for a mud volcanic origin of the mottled zone, dead sea area," *Basin Research*, vol. 22, no. 4, pp. 414–438, 2010.

[28] Y. I. Geller, A. Burg, L. Halicz, and Y. Kolodny, "System closure during the combustion metamorphic "mottled zone" event, Israel," *Chemical Geology*, vol. 334, pp. 25–36, 2012.

[29] I. Novikov, Ye. Vapnik, and I. Safonova, "Mud volcano origin of the mottled zone, South Levant," *Geoscience Frontiers*, vol. 4, no. 5, pp. 597–619, 2013.

[30] E. V. Sokol, S. N. Kokh, V. V. Sharygin, et al., "Mineralogical diversity of Ca2Si$_O$4-B$_E$Aring combustion metamorphic rocks in the Hatrurim Basin: implications for storage and partitioning of elements in oil shale Clinkering," *Minerals*, vol. 9, no. 8, p. 465, 2019.

[31] Y. Kolodny and S. Gross, "Thermal Metamorphism by combustion of organic matter: isotopic and Petrological evidence," *The Journal of Geology*, vol. 82, no. 4, pp. 489–506, 1974.

[32] E. Galuskin, I. O. Galuskina, V. Kamenetsky, et al., "First in situ terrestrial Osbornite (tin) in the Pyrometamorphic Hatrurim complex, Israel," *Lithosphere*, vol. 2022, no. 1, p. 8127747, 2022.

[33] R. Grapes, *Pyrometamorphism*, Springer-Verlag, 2006.

[34] E. V. Sokol, I. S. Novikov, Ye. Vapnik, and V. V. Sharygin, "Gas fire from mud volcanoes as a trigger for the appearance of high-temperature Pyrometamorphic rocks of the Hatrurim formation (dead sea area)," *Doklady Earth Sciences*, vol. 413, no. 2, pp. 474–480, 2007.

[35] Y. Vapnik, V. V. Sharygin, E. V. Sokol, and R. Shagam, "Paralavas in a combustion metamorphic complex: Hatrurim Basin, Israel," *Reviews in Engineering Geology*, vol. 18, pp. 1–21, 2007.

[36] I. O. Galuskina, Y. Vapnik, B. Lazic, T. Armbruster, M. Murashko, and E. V. Galuskin, "Harmunite Cafe2O4: A new mineral from the Jabel Harmun, West Bank, Palestinian autonomy, Israel," *American Mineralogist*, vol. 99, nos. 5–6, pp. 965–975, 2014.

[37] A. Krzątała, B. Krüger, I. Galuskina, Y. Vapnik, and E. Galuskin, "Walstrom$_1$te, Baca2(Si3O9), from Rankinite Paralava within Gehlenite Hornfels of the Hatrurim Basin, Negev desert, Israel," *Minerals*, vol. 10, no. 5, p. 407, 2020.

[38] A. Burg, A. Starinsky, Y. Bartov, and Y. Kolodny, "Geology of the Hatrurim formation (mottled zone) in the Hatrurim Basin," *Israel Journal of Earth Sciences*, vol. 40, pp. 107–124, 1991.

[39] Y. Kolodny, A. Burg, Y. I. Geller, L. Halicz, and Y. Zakon, "Veins in the Combusted metamorphic rocks, Israel; weathering or a retrograde event?," *Chemical Geology*, vol. 385, pp. 140–155, 2014.

[40] R. Juroszek, B. Krüger, I. Galuskina, H. Krüger, Y. Vapnik, and E. Galuskin, "Siwaqaite, Ca6Al$_2$(C$_R$O4)3(OH)12·$_{26}$H2O, a new mineral of the Ettringite group from the Pyrometamorphic Daba-Siwaqa complex, Jordan," *American Mineralogist*, vol. 105, no. 3, pp. 409–421, 2020.

[41] K. Skrzyńska, G. Cametti, I. O. Galuskina, Y. Vapnik, and E. V. Galuskin, "Sr4(AL$_8$Si8O3$_2$).$_9$H2O, a new Strontium dominant, orthorhombic Zeolite of the Gismondine series from the Hatrurim complex, Israel," *American Mineralogist*, vol. 108, no. 2, pp. 249–258, 2023.

[42] A. Matthews and S. Gross, "Petrological evolution of the "mottled zone" (Hatrurim) metamorphic complex of Israel," *Israel Journal of Earth Sciences*, vol. 29, pp. 93–106, 1980.

[43] G. M. Sheldrick, "A short history of SHELX," *Acta Crystallographica. Section A, Foundations of Crystallography*, vol. 64, no. Pt 1, pp. 112–122, 2008.

[44] L. J. Farrugia, "Wingx and ORTEP for windows: an update," *Journal of Applied Crystallography*, vol. 45, pp. 849–854, 2012.

[45] G. M. Sheldrick, "Crystal structure refinement with SHELXL," *Structural Chemistry*, vol. 71, pp. 3–8, 2015.

[46] S. N. Britvin, M. G. Krzhizhanovskaya, A. A. Zolotarev, et al., "Crystal chemistry of Schreibersite, (Fe,Ni)3P," *American Mineralogist*, vol. 106, no. 9, pp. 1520–1529, 2021.

[47] E. V. Galuskin, J. Kusz, I. O. Galuskina, M. Książek, Ye. Vapnik, and G. Zieliński, "Discovery of terrestrial Andreyivanovite, Fecrp, and the effect of Cr and V substitution in Barringerite-Allabogdanite low-pressure transition," *American Mineralogist*, vol. 108, no. 8, pp. 1506–1515, 2023.

[48] R. D. Shannon, "Revised effective ionic radii and systematic studies of Interatomic distances in halides and Chalcogenides," *Acta Crystallographica Section A*, vol. 32, no. 5, pp. 751–767, 1976.

[49] S. M. Antao and J. J. Salvador, "Crystal chemistry of Birefringent Uvarovite solid solutions," *Minerals*, vol. 9, no. 7, p. 395, 2019.

[50] A. M. Hofmeister and A. Chopelas, "Vibrational spectroscopy of end-member silicate Garnets," *Physics and Chemistry of Minerals*, vol. 17, no. 6, pp. 503–526, 1991.

[51] P. Mingsheng, H. K. Mao, L. Dien, and E. C. T. Chao, "Raman spectroscopy of garnet-group minerals," *Chinese Journal of Geochemistry*, vol. 13, no. 2, pp. 176–183, 1994.

[52] B. A. Kolesov and C. A. Geiger, "Raman spectra of silicate Garnets," *Physics and Chemistry of Minerals*, vol. 25, no. 2, pp. 142–151, 1998.

[53] A. Chopelas, "Single crystal Raman spectrum of Uvarovite, Ca3Cr$_2$SI$_3$O1$_2$," *Physics and Chemistry of Minerals*, vol. 32, nos. 8–9, pp. 525–530, 2005.

[54] T. Moroz, A. Ragozin, D. Salikhov, G. Belikova, V. Puchkov, and H. Kagi, "Micro-Raman spectra of Ugrandite garnet," *Spectrochimica Acta. Part A, Molecular and Biomolecular Spectroscopy*, vol. 73, no. 3, pp. 436–439, 2009.

[55] P. Makreski, T. Runčevski, and G. Jovanovski, "Characterization and Spectra-structure correlations for Grossular and Uvarovite. Raman study supported by IR spectroscopy," *Journal of Raman Spectroscopy*, vol. 42, no. 1, pp. 72–77, 2011.

[56] S. Kos, M. Dolenec, J. Lux, and S. Dolenec, "Raman Microspectroscopy of Garnets from S-Fibulae from the archaeological site Lajh (Slovenia)," *Minerals*, vol. 10, no. 4, p. 325, 2020.

[57] M. Fu, J. Dai, and L. Zhao, "A study on the Raman spectral characteristics of garnet from the Jiama copper Polymetallic deposit in Tibet," *Minerals*, vol. 12, no. 12, p. 1578, 2022.

[58] M. Andrut and M. Wildner, "The crystal chemistry of Birefringent natural Uvarovites: part I. optical investigations and UV-VIS-IR absorption spectroscopy," *American Mineralogist*, vol. 86, no. 10, pp. 1219–1230, 2001.

[59] G. A. Challis, R. Grapes, and K. Palmer, "Chromian Muscovite, Uvarovite, and Zincian chromite; products of regional Metasomatism in Northwest Nelson, New Zealand," *Canadian Mineralogist*, vol. 33, pp. 1263–1284, 1995.

[60] T. Pal and D. Das, "Uvarovite from chromite-bearing Ultramafic Intrusives, Orissa, India, a crystal-chemical characterization using 57Fe Mössbauer spectroscopy," *American Mineralogist*, vol. 95, nos. 5–6, pp. 839–843, 2010.

[61] G. Parthasarathy, V. Balaram, and R. Srinivasan, "Characterization of green Garnets from an Archean Calc-silicate rock, Bandihalli, Karnataka, India: evidence for a continuous solid solution between Uvarovite and Grandite," *Journal of Asian Earth Sciences*, vol. 17, no. 3, pp. 345–352, 1999.

[62] J. Willemse and J. J. Bensch, "Inclusionso Foriginal carbonate rocks in Gabbro and Norite of the Eastern part of the Bushveld complex," *South African Journal of Geology*, vol. 67, pp. 1–87, 1964.

[63] E. S. Persikov, P. G. Bukhtiyarov, L. Ya. Aranovich, A. N. Nekrasov, and O. Yu. Shaposhnikova, "Experimental modeling of formation of native metals (Fe, NI, Co) in the earth's crust by the interaction of hydrogen with Basaltic melts," *Geochemistry International*, vol. 57, no. 10, pp. 1035–1044, 2019.

[64] Y. V. Seryotkin, E. V. Sokol, and S. N. Kokh, "Natural Pseudowollastonite: crystal structure, associated minerals, and geological context," *Lithos*, vols. 134–135, pp. 75–90, 2012.

[65] W. L. Griffin, S. E. M. Gain, J.-X. Huang, et al., "A terrestrial Magmatic Hibonite-Grossite-vanadium assemblage: Desilication and extreme reduction in a volcanic plumbing system, mount Carmel, Israel," *American Mineralogist*, vol. 104, no. 2, pp. 207–219, 2019.